5. Supplementary material

5.1. Experimental Observation of Ni-film Electrode

The patterned Ni-film electrode was prepared by DC Ni sputtering method and operated in FC and EC modes under larger polarization. The morphological changes of Ni around the edge of the Ni-film after operation in 3% humidified H_2 at 800°C for 5 hours are shown in Fig. S0. Further details of the experiments are given in Ref. [1].

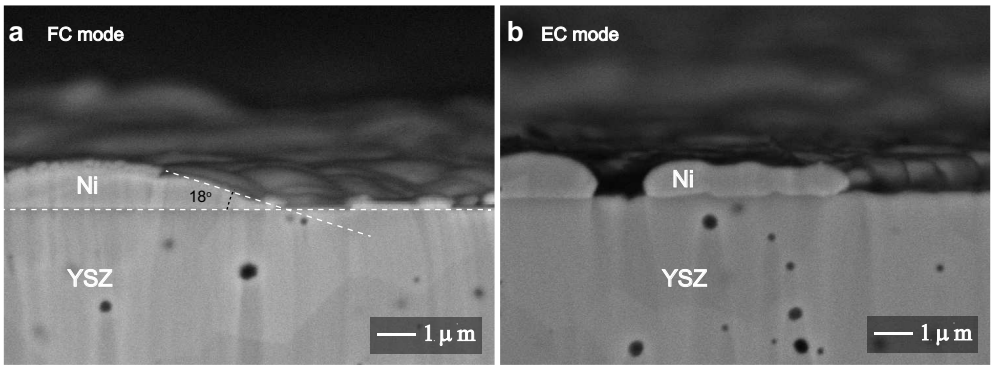

Figure S0: The SEM images of the Ni-YSZ interface cross-sections at the edges of the Ni-film after 5 hours of operation in (a) FC and (b) EC modes.

5.2. Multi-physics coupled FE modeling

To achieve the multi-physics coupled modeling in full-cell scale, the model was built based on a combination of a homogeneous HSL and heterogeneous reconstructions of HSL, HFL, electrolyte, BL, and oxygen electrode. The TPB density, volume fraction, and tortuosity factor obtained based on the 3D reconstruction of the heterogeneous HSL microstructure were used to establish the homogeneous HSL representing the remaining HSL in a large span. The microstructure reconstructions of cells A and B in full-cell scale and the corresponding meshes are shown in Fig. 2(b).

In multi-physics coupled FE modeling, governing equations for the electronic, ionic conduction, and gas

diffusion processes are expressed as

$$\begin{cases} C_{\mathrm{dl}}\frac{\partial}{\partial t}\left(\frac{\tilde{\mu}_{\mathrm{O}^{2-}}}{2F}-\frac{\tilde{\mu}_{\mathrm{e}^-}}{F}\right)-\nabla\cdot\left(\frac{\sigma_{\mathrm{O}^{2-}}}{2F}\nabla\tilde{\mu}_{\mathrm{O}^{2-}}\right)=-i_{\mathrm{reac}} \\ -C_{\mathrm{dl}}\frac{\partial}{\partial t}\left(\frac{\tilde{\mu}_{\mathrm{O}^{2-}}}{2F}-\frac{\tilde{\mu}_{\mathrm{e}^-}}{F}\right)-\nabla\cdot\left(\frac{\sigma_{\mathrm{e}^-}}{F}\nabla\tilde{\mu}_{\mathrm{e}^-}\right)=i_{\mathrm{reac}} \\ \frac{\partial c_j}{\partial t}+\nabla\cdot(D_j\nabla c_j)=s_j,\ \left(s_{\mathrm{H}_2}=\frac{i_{\mathrm{reac}}}{2F}, s_{\mathrm{O}_2}=-\frac{i_{\mathrm{reac}}}{4F}\right) \end{cases}, \tag{1}$$

where $\tilde{\mu}_{\mathrm{O}^{2-}}$, $\tilde{\mu}_{\mathrm{e}^-}$, $\sigma_{\mathrm{O}^{2-}}$, and σ_{e^-} represent the electrochemical potentials and conductivities of oxygen ions and electrons, respectively. C_{dl} is the capacitance of the heterogeneous double-layer. The effective double-layer capacitance $C^{\mathrm{eff}}_{\mathrm{dl,HSL}}$ in the HSL can be evaluated as $C^{\mathrm{eff}}_{\mathrm{dl,HSL}}=C^{\mathrm{N/Y}}_{\mathrm{dla}}S_{\mathrm{N/Y}}$, where $S^{\mathrm{N/Y}}$ is the volume-specific Ni-YSZ interfacial area. Thus, the effective oxygen ion conductivity, electron conductivity, and gas diffusion coefficients can be calculated using the corresponding volume fraction V_j and the tortuosity factor τ_j of phase j as

$$\Gamma^{\mathrm{eff}}_j=\frac{V_j}{\tau_j}\Gamma_j\,(\Gamma_j=\sigma_{\mathrm{O}^{2-}},\sigma_{\mathrm{e}^-},D_{\mathrm{H}_2,\mathrm{H}_2\mathrm{O}},D_{\mathrm{H}_2,\mathrm{kn}}). \tag{2}$$

F is the Faraday constant, i_{reac} is the stable Faraday current density associated with the sustained electrochemical reactions at TPBs or double-phase-boundaries (DPBs), c_j is the molar concentration of gas species j, and s_j is the volumetric specific molar consumption rate of gas species j in the electrochemical reactions. The corresponding gas diffusivity D_j can be calculated based on a simplified dust gas model (DGM) as

$$D_j=\left(\frac{1-\alpha y_j}{D_{j,k}}+\frac{1}{D_{j,\mathrm{kn}}}\right)^{-1}, \tag{3}$$

with the binary diffusion coefficient $D_{j,k}$ and the Knudsen diffusion coefficient $D_{j,\mathrm{kn}}$ defined as

$$\begin{cases} D_{j,k}=0.0005956\sqrt{\frac{1}{M_j}+\frac{1}{M_k}}\frac{T^{3/2}}{P_t\Omega_{\mathrm{D}}\zeta^2_{j,k}} \\ D_{j,\mathrm{kn}}=\frac{2}{3}r\sqrt{\frac{8RT}{\pi M_j}} \end{cases}, \tag{4}$$

where M_j is the molecular weight of the gas species j, P_{t} is a constant total pressure, T is a constant temperature, and $\alpha=1-\sqrt{\frac{M_j}{M_k}}$. The intermolecular force constant $\zeta_{j,k}$ was taken as the arithmetic mean of ζ_j and ζ_k. The collision integral is defined as $\Omega_{\mathrm{D}}=1.1336\left(\frac{Tk}{\varepsilon}\right)^{-0.1814}$, where ε is the geometric mean value.

The electrochemical reactions in the hydrogen electrode occur only at Ni-YSZ-pore TPBs, while the electrochemical reactions in the oxygen electrode occur simultaneously at the LSCF-GDC DPBs and LSCF-GDC-pore TPBs. The corresponding local electrochemical reaction current density integrals at the heterogeneous boundary and interface, as well as the current density in the homogeneous HSL, can be calculated using a group of Butler-Volmer equations as

$$\begin{cases} \lim\limits_{\delta S\to 0}\int i_{\mathrm{reac,TPB,fuel}}\mathrm{d}S = i_{0,\mathrm{TPB,a}}\left[\exp\left(\frac{2.0F}{RT}\eta_{\mathrm{act,fuel}}\right)-\exp\left(-\frac{1.0F}{RT}\eta_{\mathrm{act,fuel}}\right)\right] \\ \lim\limits_{\delta S\to 0}\int i_{\mathrm{reac,TPB,O_2}}\mathrm{d}S = i_{0,\mathrm{TPB,O_2}}\left[\exp\left(\frac{2.0F}{RT}\eta_{\mathrm{act,O_2}}\right)-\exp\left(-\frac{2.0F}{RT}\eta_{\mathrm{act,O_2}}\right)\right] \\ \lim\limits_{\delta l\to 0}\int i_{\mathrm{reac,DPB,O_2}}\mathrm{d}l = i_{0,\mathrm{DPB,O_2}}\left[\exp\left(\frac{1.2F}{RT}\eta_{\mathrm{act,O_2}}\right)-\exp\left(-\frac{1.0F}{RT}\eta_{\mathrm{act,O_2}}\right)\right] \\ i_{\mathrm{reac,HSL}} = i_{0,\mathrm{TPB,fuel}}l_{\mathrm{TPB,HSL}}\left[\exp\left(\frac{2.0F}{RT}\eta_{\mathrm{act,fuel}}\right)-\exp\left(-\frac{1.0F}{RT}\eta_{\mathrm{act,fuel}}\right)\right] \end{cases}, \tag{5}$$

where $i_{0,\mathrm{TPB,fuel}}$, $i_{0,\mathrm{TPB,O_2}}$, and $i_{0,\mathrm{DPB,O_2}}$ are exchange-current densities at TPBs in hydrogen electrode, at TPBs and DPBs in oxygen electrode, respectively. $i_{\mathrm{reac,HSL}}$ is the volume specific electrochemical reaction current in the HSL.

5.3. Multi-physics coupled PF modeling

Based on the results of the multi-physics coupled FE simulation, the microstructure evolutions in the Ni-YSZ composite hydrogen electrode during operation in different modes for both cells A and B were simulated using PFM. A unique resolution of $180 \times 200 \times 180$ discrete voxels was used in the simulations, with a length of about 10 voxels belonging to electrolyte and the rest belonged to electrode. Phases Ni and YSZ were introduced in PF modeling using two OPs, i.e. $\phi^{\mathrm{N}}(\boldsymbol{r})$ and $\phi^{\mathrm{Y}}(\boldsymbol{r})$, where $\boldsymbol{r}$ is a spatial parameter. $\phi^{\mathrm{N/Y}}(\boldsymbol{r}) = 1$ was set in solid phase, and $\phi^{\mathrm{N/Y}}(\boldsymbol{r}) = 0$ outside. The pore phase can be determined as $\phi^{\mathrm{P}}(\boldsymbol{r}) = 1 - \phi^{\mathrm{N}} - \phi^{\mathrm{Y}}$. Moreover, the crystallographic orientations in a given solid phase were defined using OPs as $[\eta_1(\boldsymbol{r}), \eta_2(\boldsymbol{r}), \ldots, \eta_q(\boldsymbol{r})] = (\pm 1.0, 0, \ldots, 0), (0, \pm 1.0, \ldots, 0), \cdots (0, 0, \ldots, \pm 1.0)$, where q is the number of crystallographic orientations for both the Ni phase and the YSZ phase, while ± 1.0 indicates two

different crystallographic orientations in one orientation OP. The total free energy of the system can thus be expressed as

$$F = \int_V dV \left\{ \Delta f f_0 \left(\phi^{\mathrm{N}}, \phi^{\mathrm{Y}}, \eta_j^{\mathrm{N}}, \eta_j^{\mathrm{Y}}\right) + \sum_{p=\mathrm{N}}^{\mathrm{Y}} \left[\frac{\kappa_\phi^p}{2} (\nabla \phi^p)^2 + \sum_{j=1}^{q} \frac{\kappa_j^p}{2} \left(\nabla \eta_j^p\right)^2 \right] \right\}, \tag{6}$$

where κ_ϕ^p and κ_j^p are the corresponding coefficients of the gradient energy of the material surface and grain boundary. Thus, the free energy density of the system f_0 is composed of the contributions from the various interfaces and the electromigration driving force on the Ni phase subjected to a current density [38, 39], which is defined as

$$f_0 = \Delta f \left\{ \sum_{p=\mathrm{N}}^{\mathrm{Y}} \left[f_1\left(\phi^p\right) + \sum_{j=1}^{q} f_2\left(\phi^p, \eta_j^p\right) + \sum_{j=1}^{q} \sum_{k \neq j}^{q} f_3\left(\eta_j^p, \eta_k^p\right) \right] + f_4\left(\phi^{\mathrm{N}}, \phi^{\mathrm{Y}}\right) + f_5\left(\phi^{\mathrm{N}}, \phi^{\mathrm{Y}}\right) \right\} + f_6\left(\phi^{\mathrm{N}}, \mu^{\mathrm{N}}\right), \tag{7}$$

where Δf is a common coefficient of the interfacial energy densities and

$$\begin{cases} f_1\left(\phi^x\right) = -\left(A/2\right)\left(\phi^x - \phi^m\right)^2 + \left(B/4\right)\left(\phi^x - \phi^m\right)^4 + \left(D/4\right)\left(\phi^x - \phi^0\right)^4 \\ f_2\left(\phi^x, \eta_j^x\right) = -\left(\gamma/2\right)\left(\phi^x - \phi^0\right)^2 \left(\eta_j^x\right)^2 + \left(\gamma/4\right)\left(\eta_j^x\right)^4 \\ f_3\left(\eta_j, \eta_k\right) = \left(\varepsilon_{jk}/2\right)\left(\eta_j\right)^2 \left(\eta_k\right)^2 \\ f_4\left(\phi^x, \phi^y\right) = \left(\lambda/2\right)\left(\phi^x\right)^2 \left(\phi^y\right)^2 \\ f_5\left(\phi^x, \phi^y\right) = -W\phi^x \left|\nabla \phi^y\right|^2 \\ f_6\left(\phi^x, \mu^x\right) = -H\phi^x \mu^x \end{cases}, \tag{8}$$

where f_1, f_2, f_3 and f_4 correspond to a volume fraction-dependent double-well potential function, the mutual coupling effects among the volume fractions and the crystallographic orientations of different phases, respectively. f_5 denotes a term related to the wettability of Ni on YSZ. The coefficient H in f_6, defined as $H = \frac{N_a |e| Z^*}{F}$, is a fixed value describing an electromigration-induced driving force exerted on Ni by the electron wind force along a current driven by an electrochemical potential gradient [38, 39]. N_a is the number of Ni atoms per unit volume, e is the charge of an electron, and Z^* is the effective valence of the

Ni atom. The driving force can thus be related to the electrochemical potential field μ^{N} generated in the multi-physics coupled FE simulation.

To facilitate the simulation, YSZ was set as a stable phase due to its low diffusion coefficient at the operating temperature [40], which is also consistent with the experimental observation [41]. The conserved Cahn-Hilliard dynamic evolution equation was utilized as the governing equation to predict Ni phase evolution as

$$\frac{\partial \phi^{\mathrm{N}}}{\partial t} = \nabla \cdot \left[M \nabla \left(\frac{\partial f_0}{\partial \phi^{\mathrm{N}}} - \kappa_{\phi}^{\mathrm{N}} \nabla^2 \phi^{\mathrm{N}} \right) \right] \tag{9}$$

where t is time and M is the mobility of Ni phase, which is defined as

$$M = M_{\phi}^{\mathrm{N}} \left[M_{\mathrm{vol}}^{*} h\left(\phi^{\mathrm{N}}\right) + M_{\mathrm{surf}}^{*} \phi^{\mathrm{N}} \left(1 - \phi^{\mathrm{N}}\right) + M_{\mathrm{gb}}^{*} \sum_{j}^{p} \sum_{k \neq j}^{p} \left| \eta_j^{\mathrm{N}} \eta_k^{\mathrm{N}} \right| \right] g\left(1 - \phi^{\mathrm{Y}}\right), \tag{10}$$

where $h(x) = x^3 \left(10 - 15x + 6x^2\right)$, $g(x) = x^6 \left(10x^2 - 15x + 6\right)$ are two interpolation functions used to limit the mobility of Ni in bulk and at Ni-YSZ interface. In addition, M_{ϕ}^{N} is an unknown composition coefficient of Ni under a specific operation conditions, and the dimensionless coefficients $M_{\mathrm{vol}}^{*} = 0.01$, $M_{\mathrm{surf}}^{*} = 4$ and $M_{\mathrm{gb}}^{*} = 0.4$ are related to the bulk, the surface and grain boundary of Ni, respectively.

Based on the Allen-Cahn dynamics evolution equation, non-conserved governing equations of Ni crystal grain growth can be defined as

$$\frac{\partial \eta_j^{\mathrm{N}}}{\partial t} = -L_j \left(\frac{\partial f_0}{\partial \eta_j^{\mathrm{N}}} - \kappa_j^{\mathrm{N}} \nabla^2 \eta_j^{\mathrm{N}} \right); j = 1, 2, \ldots, q \tag{11}$$

where L_j is the mobility of Ni grain boundary. To facilitate the calculation, the value of L_j was assumed to be identical for each crystallographic orientation. The fourier-spectral method was utilized to solve the partial differential equations, and periodic boundary conditions were applied along the three axes in all simulations. The phenomenological parameters in Eq. (8) were chosen as $\phi_m = 0.5$, $\phi_0 = 0$, $A = 1.0$,

$B = 4.0$, $D = 1.0$, $\gamma = 1.0$, $\varepsilon_{jk} = 3.0$, and $\lambda = 1.19$. Gradient coefficients were chosen as $\kappa_\phi^{\mathrm{N}} = 1$, $\kappa_\phi^{\mathrm{Y}} = 0.82$, $\kappa_j^{\mathrm{N}} = 0.71$, and $\kappa_j^{\mathrm{Y}} = 0.52$ [33, 42]. A dimensionless coefficient $H^* = \frac{H\mu_{\max}}{\Delta f}$ was set to 250 in f_6 to control the electromigration driving force. After non-dimensionalizing the other relevant parameters and the governing equations, a semi-implicit scheme was applied to alleviate the time-step constraint without loss of stability or accuracy, with the further details are given in Refs. [20, 33].

5.4. MD Modeling

As a common interfacial combination between Ni and YSZ, the Ni[111]/YSZ[111] interface was chosen as a representative example in the present MD simulations, as shown in Fig. S1. The YSZ model was constructed by randomly replacing Zr^{4+} with Y^{3+} in ZrO_2. To keep the charge neutral, one O^{2+} was randomly deleted in the model when two Zr^{4+} ions were replaced [2]. In addition, the YSZ layer with doping concentration ranging from 1mol% (1YSZ) to 35mol% (35YSZ) was used to investigate the effects of doping concentration on the interfacial bonding properties. The sizes of YSZ and Ni in the Ni-YSZ supercell were chosen so that the lattice mismatch at the interface was less than 3%. Periodic boundary conditions were applied in all directions. A vacuum layer with a thickness of 20 Å was added along the z-axis to avoid the repeated interface caused by periodicity. All simulations were performed in the LAMMPS package [3]. A recently developed ReaxFF potential was used to describe the formation of the Ni-YSZ interface [4], which contains the bond order to describe the formation and breaking of chemical bonds. The ReaxFF potential can well simulate Ni-O bond formation at Ni-YSZ interfaces, which is not possible with conventional potentials. To obtain a stable interface, the Ni-YSZ system was first relaxed at the corresponding temperature using the isothermic-isobaric (NPT) ensemble to relieve the stress, and then switched to the isothermic-isochoric (NVT) ensemble to allow the system to reach a steady state. The binding properties of the Ni-YSZ interfaces were then analyzed.

The stability of the Ni-YSZ interfaces was verified by the convergence of the system energy, as shown in Fig. S2(a). Since the Ni-O bond is the predominant chemical bond at the Ni-YSZ interface, we show in

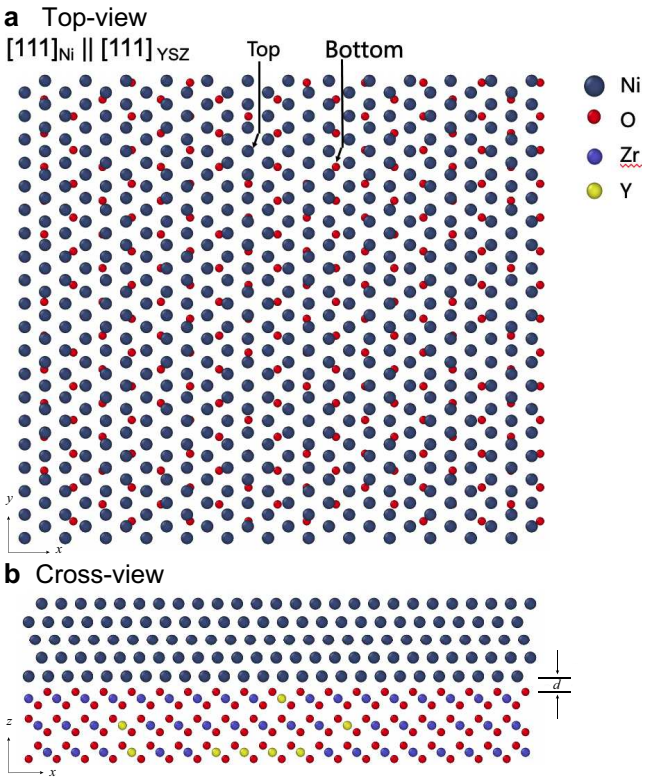

Figure S1: The model of Ni-YSZ interface used in the MD simulation.

Fig. S2(b) the evolution of the interfacial O atoms bonded to Ni atoms during the MD simulations, which was measured as the fraction of the number of bonded O atoms in the total number of O atoms in YSZ surface. It was found that the fraction of O atoms bonded in all Ni-YSZ interface models remained almost unchanged at the end of the MD simulations, which indicates the stability of the Ni-YSZ interfaces obtained. Based on Fig. S2(b), the fractions of bonded O atoms at different Ni-YSZ interfaces with different doping concentrations in YSZ are plotted in Fig. S3(a). It can be seen that the fraction of bonded O atoms decreases from 0.90 in the Ni-1YSZ interface to 0.69 in its Ni-35YSZ counterpart, indicating that the number of Ni-O bonds decreases with the increase of doping concentration. Therefore, it is expected that the bond strength of the Ni-YSZ interface becomes weaker as the doping concentration of YSZ increases. Figure S3(b) shows the defect fraction at the interface of all Ni-YSZ models. It is defined as the ratio between the number of O vacancies in the inner surface of YSZ to the number of O atoms in the perfect ZrO_2 surface. It is found that the interfacial defect fraction of the Ni-YSZ structure generally increases as the doping concentration increases. Thus, the decrease in the number of interfacial O atoms in this process is responsible for the lower number of Ni-O bonds formed at a higher doping concentration.

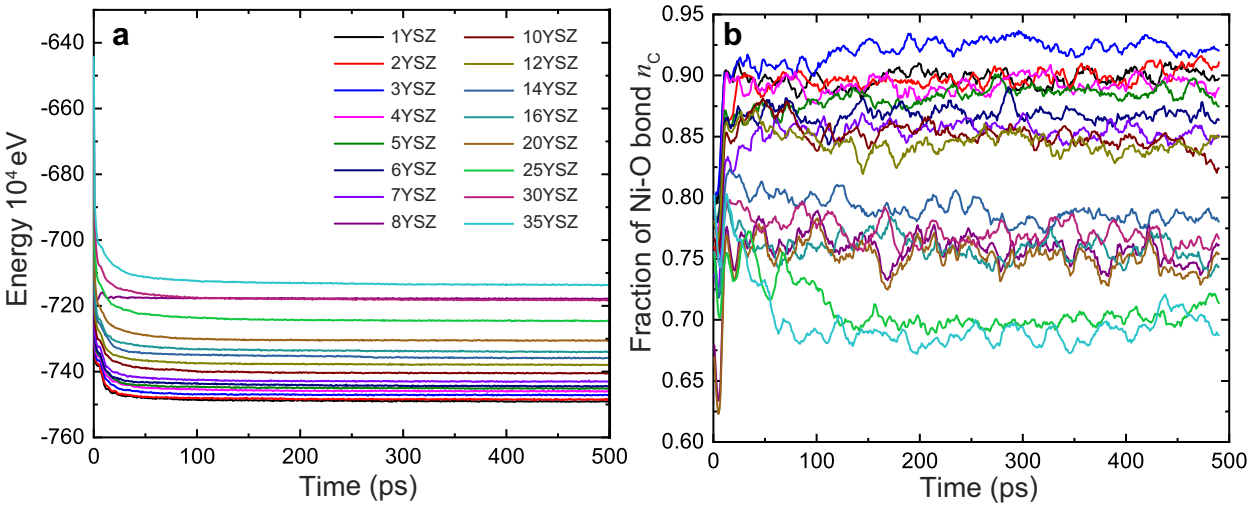

Figure S2: (a) Energy change and (b) evolution of fraction of bonded O atoms during the simulation process.

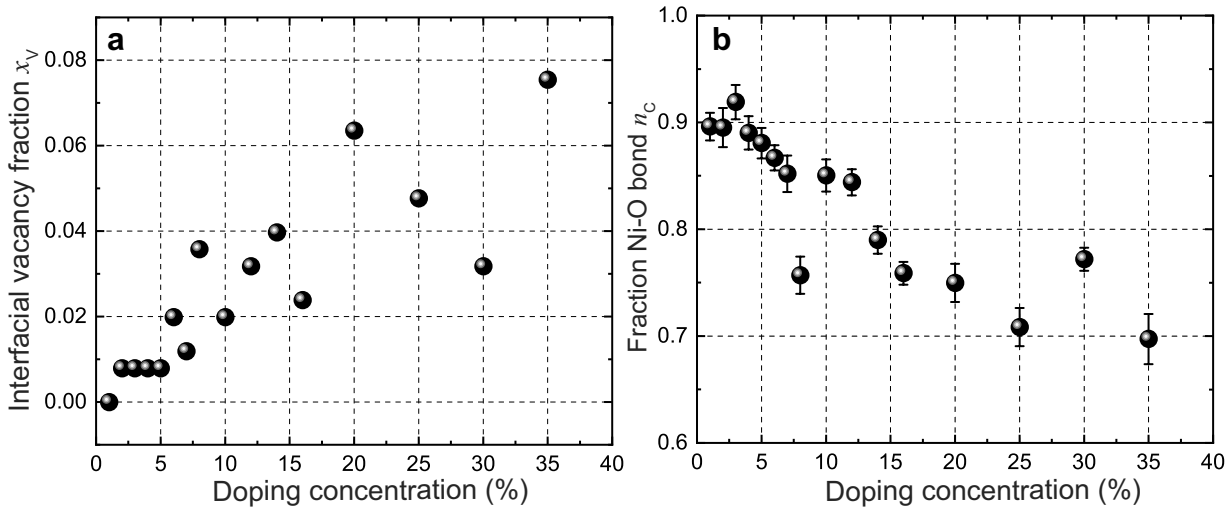

Figure S3: Fractions of (a) bonded O atoms and (b) interfacial defect of YSZ versus yittria-doping concentrations.

References

[1] Z. Jiao and N. Shikazono, Study on the effects of polarization on local morphological change of nickel at active three-phase-boundary using patterned nickel-film electrode in solid oxide fuel cell anode, Acta Materialia, 135 (2017) 124–131.

[2] P. K. Schelling and S. R. Phillpot, Mechanism of Thermal Transport in Zirconia and Yttria-Stabilized Zirconia by Molecular-Dynamics Simulation, Journal of the American Ceramic Society,84(12) (2001) 2997–3007.

[3] D. M. Beazley, P. S. Lomdahl, N. Gronbech-Jensen, et al., Parallel Algorithms for Short-Range Molecular Dynamics, Annual Reviews of Computational Physics III, (1995) 119–175.

[4] B. V. Merinov, J. E. Mueller, A. C. T. Van Duin, et al., ReaxFF Reactive Force-Field Modeling of the Triple-Phase Boundary in a Solid Oxide Fuel Cell, The Journal of Physical Chemistry Letters, 5(22) (2014) 4039–4043.